Low dose oral corticosteroids in asthma associates with increased morbidity and mortality

Skov, Inge Raadal; Madsen, Hanne; Henriksen, Daniel Pilsgaard; Andersen, Jacob Harbo; Pottegård, Anton; Davidsen, Jesper Rømhild

Published in:
European Respiratory Journal

DOI:
10.1183/13993003.03054-2021

Publication date:
2022

Document version:
Accepted manuscript

Citation for pulished version (APA):
Skov, I. R., Madsen, H., Henriksen, D. P., Andersen, J. H., Pottegård, A., & Davidsen, J. R. (2022). Low dose oral corticosteroids in asthma associates with increased morbidity and mortality. *European Respiratory Journal*, *60*(3), Article 2103054. https://doi.org/10.1183/13993003.03054-2021

60-nm-Span Wavelength-Tunable Vortex Fiber Laser with Intracavity Plasmon Metasurfaces

Lili Gui,[1,†,*] Chuanshuo Wang,[1,2,†] Fei Ding,[2] Hao Chen,[1] Xiaosheng Xiao,[1] Sergey I. Bozhevolnyi,[2] Xiaoguang Zhang,[1] and Kun Xu[1,*]

[1]State Key Laboratory of Information Photonics and Optical Communications, Beijing University of Posts and Telecommunications, Beijing 100876, China

[2]Centre for Nano Optics, University of Southern Denmark, Campusvej 55, Odense M DK-5230, Denmark

[*]Corresponding author: liligui@bupt.edu.cn; xukun@bupt.edu.cn

ABSTRACT: Wavelength-tunable vortex fiber lasers that could generate beams carrying orbital angular momentum (OAM) hold great interest in large-capacity optical communications. The wavelength tunability of conventional vortex fiber lasers is however limited by the range of ~ 35 nm due to narrow bandwidth and/or insertion loss of mode conversion components. Optical metasurfaces apart from being compact planar components can flexibly manipulate light with high efficiency in a broad wavelength range. Here, we propose and demonstrate for the first time, to the best of our knowledge, a metasurface-assisted vortex fiber laser that can directly generate OAM beams with customizable topological charges. Due to the designed broadband gap-surface plasmon metasurface, combined with an intracavity tunable filter, the laser enables OAM beam with center wavelength continuously tunable from 1015 nm to 1075 nm, nearly twice of other vortex fiber lasers ever reported. The metasurface can be designed at will to satisfy requirements for either low pump threshold or high slope efficiency of the laser. Furthermore, the cavity-metasurface configuration can be extended to generate higher-order OAM beams or more complex structured beams in different wavelength regions, which greatly broadens the possibilities for developing low-cost and high-quality structured-beam laser sources.

KEYWORDS: light manipulation, plasmon metasurface, orbital angular momentum (OAM), vortex fiber laser, wavelength-tunable

INTRODUCTION

Vortex beam carrying orbital angular momentum (OAM) possesses a spiral wavefront with a phase singularity in its center in addition to the doughnut-like annular intensity pattern.[1,2] The phase distribution contains an $\exp(il\varphi)$ phase factor, where φ is the azimuthal angle around the optical axis, and l is the topological charge, which describes the phase variation period of the beam along the transverse section. Different OAM modes are orthogonal to each other, enabling increased information capacity of optical communications with OAM-multiplexing.[3–6] Additionally, vortex beams hold great promise in various applications such as super-resolution microscopy,[7–10] optical tweezers and manipulation,[11–14] quantum entanglement,[15,16] and precision manufacturing.[17]

Methods for generating vortex beams can be classified into two categories, namely, with external or internal locations of vortex forming components with respect to laser cavities. In the first category, the vortex components are utilized outside the laser cavities and can be of different nature, such as spiral phase plates,[16,18,19] fork gratings,[20,21] spatial light modulators,[22,23] and q-plates.[24,25] These optical components are usually bulky and/or lossy, which makes them unfavorable for integrated and compact solutions in majority of applications. In this respect, the attention has recently been turned to optical metasurfaces – ultrathin planar components, utilizing surface nanostructures designed for shaping reflected and transmitted optical fields, that are found numerous applications ranging from beam steering to holography.[26–31] The compactness and design flexibility make metasurfaces promising candidates also for generation of optical vortices. Indeed, both plasmonic[32,33] and dielectric[34–36] metasurfaces have shown intriguing features and opened fascinating perspectives. In particular, gap-surface plasmon (GSP) metasurfaces, consisting of metal nanostructures atop an ultrathin dielectric layer supported by an optically thick metal film, are attractive due to the simplicity of their fabrication, requiring only a single-step lithography, and high operation efficiency, also when used for the vortex beam generation.[37–39]

Vortex beams generated by optical elements outside laser cavities usually suffer from limited efficiency and functionality. With optical components generating OAM beams inside laser cavities, vortex laser sources become more efficient, compact, and user-friendly. For example, the losses of intracavity mode conversion components (if needed) can be compensated by laser gain.[40,41] ensuring highly efficient OAM beam generation. Up till now, vortex microlasers,[42] solid-state lasers,[43–45] and fiber lasers[46,47] have been investigated and demonstrated extensively. Microlasers provide the most compact solutions, while solid-state lasers and fiber lasers are more mature and more versatile, concerning the well-developed usable optical components for

solid-state and fiber lasers. In order to facilitate compactness and functionalities of the vortex solid-state lasers, several pioneering works have incorporated metasurfaces into cavities to achieve high-quality OAM beams.[48–50] By intelligent design of both metasurface and cavity, Sroor et al. have demonstrated a vortex laser at visible wavelength (Nd:YAG as the gain medium and KTP crystal for second-harmonic) that delivers OAM beams of high purity up to 92%.[50]

In comparison with solid-state lasers, fiber lasers have advantages of easy alignment, compactness, high gain, low cost, and efficient heat dissipation. Vortex fiber lasers[51] employ mode-selective couplers,[52,53] few-mode long-period fiber gratings,[54] vortex waveplates,[55] spatial light modulators,[47] and offset-splicing[56] in order to implement mode selection or conversion from LP_{01} mode (the eigenmode of single-mode fiber). Unfortunately, the aforementioned optical components either exhibit narrowband operation, or induce intrinsically high loss, thus limiting the wavelength tunability (typically, span of several nanometers[54] or about 35 nm[47,57]) as well as the efficiency of vortex lasers. On one hand, wavelength tunability is of significance in applications of optical vortices including sensing and measurement, particularly in large-capacity optical communications that rely on dense multiplexing of both wavelength and OAM modes. On the other hand, slope efficiency is generally an important factor to evaluate laser performances. Hence, wavelength-tunable vortex fiber lasers with wide spectral tuning range as well as high work efficiency are greatly desired. As such, metasurfaces featuring both broadband and efficient light manipulation could potentially be the ideal choice for intracavity mode regulation of fiber lasers.

In this paper, we propose and demonstrate a vortex fiber laser with the record-wide wavelength tuning range, to the best of our knowledge, by incorporating plasmonic GSP metasurfaces with broadband beam shaping capability (continuously tunable within a wavelength span of 60 nm). GSP metasurfaces with different polarization conversion efficiencies are designed and fabricated, which enable the generation of vortex beams with topological charge of $l = \pm 1$ in the cross-polarized channel. An ytterbium-doped fiber laser with a simple linear-cavity configuration is then built, which shows a low pump threshold and decent slope efficiency (about 15%). When inserting a tunable filter inside the cavity, the center wavelength can be easily and stably tuned from 1015 nm to 1075 nm. The laser exhibits several attractive features, including compactness, easy handling and stable output free of mode competition, in addition to excellent OAM beam purity (up to ~94%). Our concept of the metasurface and cavity design greatly broadens the strategy of generating OAM beams directly at the light sources and can easily be extended to other situations, including the generation of

more complex structured beams and design of other fiber lasers working at different wavelengths.

■ RESULTS AND DISCUSSION

The Vortex Fiber Laser Cavity. In order to generate vortex beams directly from the fiber laser in the most efficient, cost-effective, and stable way, we designed the linear cavity as shown in Figure 1. The cavity basically concerns the optical properties of the metasurfaces and the guided mode of the fibers, and is thereby a hybrid vortex laser consisting of free-space components and optical fibers. One end of the cavity is a GSP metasurface in reflection, acting as not only an OAM beam converter but also an effective output coupler (assisted by a polarization beam splitter). Note that we use purely single-mode passive and active fibers in the laser, so that an LP_{01} mode exists in the fibers that is almost equivalent to a Gaussian beam. In the built cavity, a 976 nm pump source is coupled into the loop through a wavelength division multiplexer (WDM). A segment of 0.6-m ytterbium-doped polarization-maintaining fiber (Yb-PMF, NUFERN-PM-YSF-HI-HP) is used as the gain medium. A collimator emits light in parallel, bridging the fiber part and the free-space part. Since the guided light in the polarization-maintaining fibers is linearly polarized, it is only necessary to rotate the collimator in the *x*-*y* plane (also see the definition of the *x*-*y* plane in Figure 2b) to ensure that the beam emitted from the collimator is an *x*-polarized Gaussian beam, so as to minimize intracavity loss. The *x*-polarized Gaussian beam can directly pass through a polarization beam splitter (PBS) and be focused on the metasurface by an achromatic lens. Based on the mechanism of partial orthogonal linear-polarization conversion along with the phase modulation of the metasurface (see more details on metasurface design in Figure 2), the beams reflected from the metasurface contain both a *y*-polarized vortex beam and an *x*-polarized beam with unchanged polarization state (here we call co-polarized residual beam, or shortly CPR beam). After passing through the lens again, the reflected beams can be transmitted in parallel. Because the polarization states of the two beams are orthogonal to each other, the *y*-polarized vortex beam generated by the metasurface can be coupled out of the cavity through the PBS, and the transverse intensity distribution of the output vortex beam can be directly imaged by a charge-coupled device (CCD). The CPR beam is coupled back into the fiber path through the collimator. The polarization-maintaining fiber mirror at the other end of the laser does not change the polarization state of the reflected light. Therefore, the beams in the cavity can oscillate back and forth between the fiber mirror and the metasurface to form a self-consistent propagation. In order to verify the broadband manipulation of the metasurface and the wavelength tunability

of the laser, we incorporated a tunable filter (red dashed box) between the collimator and the Yb-PMF in the cavity. The wavelength of the emitted OAM beams can be continuously adjusted by switching the center wavelength of the tunable filter.

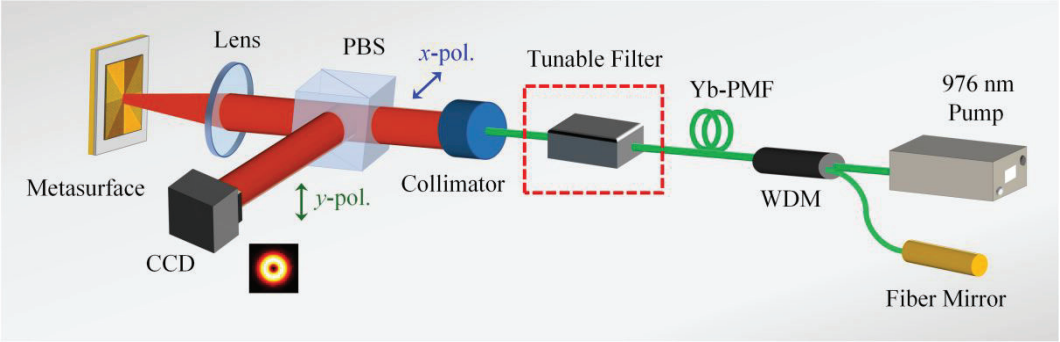

Figure 1. The hybrid vortex fiber laser with an intracavity plasmonic metasurface. WDM, wavelength division multiplexer; Yb-PMF, ytterbium-doped polarization-maintaining fiber; PBS, polarization beam splitter; CCD, charge-coupled device.

Design and Fabrication of GSP Metasurfaces. The schematic diagram of vortex beam generation with the proposed GSP metasurface is illustrated in Figure 2a. When a linearly polarized Gaussian beam (denoted as the *x*-polarized) is normally incident on our metasurface, the *y*-polarized reflected beam carrying additional phase shifts will be generated, due to the partial orthogonal linear-polarization conversion along with the phase modulation, resulting in a vortex beam with the donut-shaped intensity distribution at the cross-polarization. Figure 2b shows the building block of our proposed metasurfaces with a metal-insulator-metal (MIM) configuration. The metasurface unit consists of a gold (Au) nanorod tilted by 45° with respect to the *x*-axis on a silicon dioxide (SiO_2) spacer layer with an Au thin film at the bottom. The period of the metasurface unit in both *x*- and *y*-directions is p = 550 nm. The length (m) and width (n) of Au nanorods are variable. Since the incident linearly-polarized light may excite both the long- and short- axis electric-dipole oscillations of Au nanorods, the co- and cross-polarized light components can be generated simultaneously[58]. This metasurface configuration provides an excellent solution to generate cross-polarized OAM light with controllable conversion efficiency.

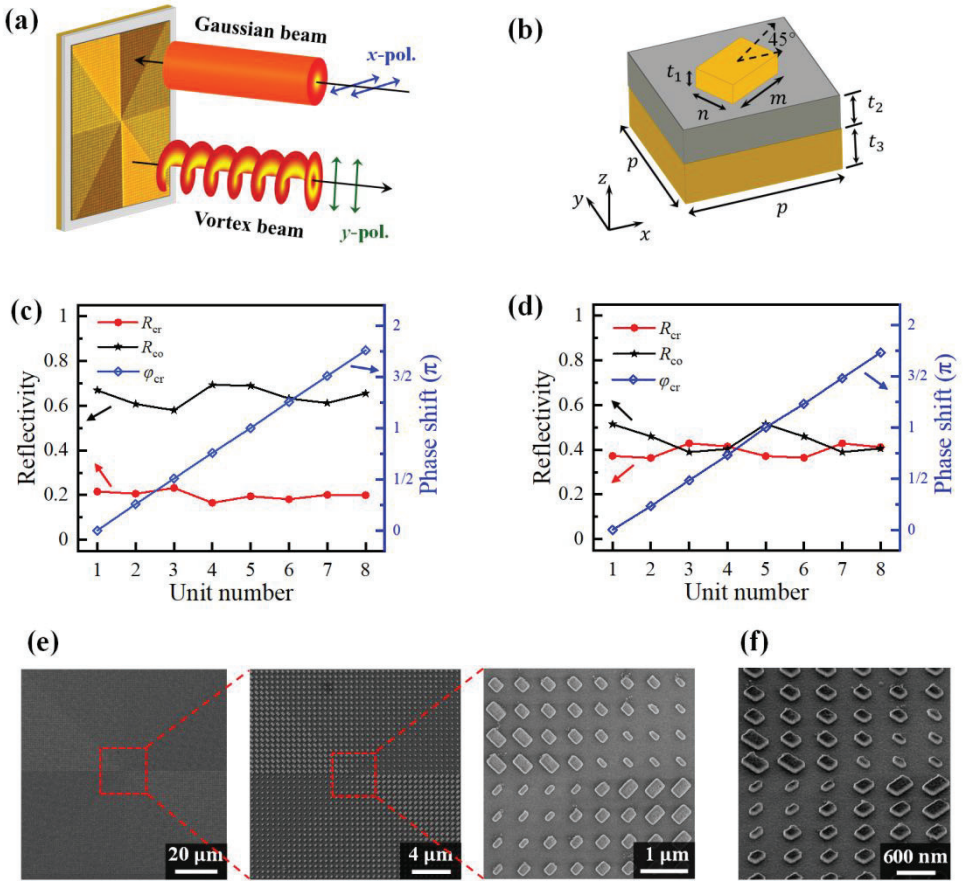

Figure 2. Metasurface design for vortex beam generation. (a) Schematic of vortex beam generation via the metasurfaces for linear-polarization conversion. (b) Schematic of the fundamental unit structure of the metasurfaces, which consists of a gold (Au) nanorod tilted by 45° with respect to the *x*-axis on a silicon dioxide (SiO_2) spacer layer with an Au thin layer at the bottom. The thicknesses of three layers are t_1= 80 nm, t_2= 110 nm, and t_3= 130 nm. The period in both *x*- and *y*-directions is p = 550 nm. The length (m) and width (n) of the nanorods are variable. (c), (d) Simulation results of the metasurface units for generating vortex beams with $l = \pm 1$. In (c) the cross-polarized reflectivity (R_{cr}) is designed to be around 20% and in (d) R_{cr} is 40%. The simulation was performed at λ = 1030 nm to match the laser wavelength. (e) Top views of scanning electron micrographs of the fabricated metasurface with R_{cr} = 40% and for $l = -1$. (f) Tilted view of the central nanorods of the above metasurface.

Based on the finite element method, we simulated the reflectivity and the phase of the periodic nanostructures consisting of the unit cell in Figure 2b, with an incident plane wave at the wavelength of λ = 1030 nm. The dielectric constant of gold is based on Lorentz-Drude model,[59] and SiO_2 is regarded as a lossless dielectric with a refractive index of ~ 1.45. By scanning the length (m) and the width (n) of the Au nanorods, the cross-polarized reflectivity (R_{cr}), co-polarized reflectivity (R_{co}), and phase shift (φ_{cr}) of the cross-polarized reflected light

were calculated versus the geometrical parameters (Figure S1). Note that the reflectivity of the cross-polarized light can potentially reach a high level (up to ~ 80%[38]) due to the Fabry-Pérot-like operation, but one should choose the cross-polarized reflectivity with care, ensuring that enough light is fed back into the laser cavity. The cross-polarized channel producing the vortex beam can be considered as a loss channel in the cavity design, with a very high cross-polarized reflectivity resulting in a cavity that requires a pretty large pump power to reach the lasing threshold. On the other hand, a very low cross-polarized reflectivity would result in a rather weak output power and inefficient generation of a vortex beam. This trade-off should be borne in mind when designing the vortex laser, suggesting the use of metasurfaces with different cross-polarized reflectivities to achieve the laser performance as needed.

Here, we first select four sets of proper nanostructures of (*m, n*) combinations that exhibit cross-polarized reflectivity (R_{cr}) of around 20% and simultaneously phase increment of $\pi/4$ for every combination sequentially, for the purpose of generating OAM beams with topological charge of one. Then we rotate the four sets of nanostructures by 90° along the *z*-axis, so that the phase shift can gain an additional value of π.[26] In this way, the eight metasurface units we selected can achieve a nearly constant cross-polarized reflectivity of ~ 20% and full phase coverage in the 2π range as shown in Figure 2c (Specific dimensions in Table S1). Similarly, we also picked other basic units with a higher cross-polarized reflectivity R_{cr} of ~ 40% to compile the metasurface with a practically constant cross-polarized reflectivity of ~ 40% as shown in Figure 2d.

We arranged the eight sets of nanorods in Figure 2c [or 2d] in counterclockwise or clockwise fashion, so as to obtain $\pm 2\pi$ phase variation along the azimuthal direction. Based on this, four metasurfaces were fabricated that enable generation of vortex beams with topological charges of $l = \pm 1$ and conversion efficiency of 20% and 40% (Figure S2). The fabrication involved a single-step electron-beam lithography. The size of each metasurface is 100 μm × 100 μm. Figure 2e,f depicts the scanning-electron microscope (SEM) images of the metasurface with R_{cr} = 40% and $l = -1$. We can clearly observe the arrangement of eight periodic arrays composed of nanorods with distinct sizes. We experimentally measured the efficiencies of the four fabricated samples outside the cavity at 1030 nm, giving rise to roughly 10% less efficiency compared with the simulated values (Figure S3). The degradation of the performances mainly stems from fabrication imperfections as well as mismatch of dielectric constant of the materials between simulation and experiment. Meanwhile, we experimentally measured the intensity of the CPR beam (Figure S4), showing that it is not a perfect Gaussian beam. When the CPR beam is coupled back to the fiber path through the collimator, it is gradually converted to the perfect

LP_{01} mode due to the mode filtering effect of the single-mode fiber. Note that a deviation of the CPR beam from a perfect LP_{01} mode leads to some extra loss in the cavity, but not too much (roughly 40% additional coupling loss in comparison to a Gaussian beam, see Figure S5 for more details).

Results of the Hybrid Vortex Laser. First, we observed the output performances of the vortex fiber laser based on four different metasurfaces without the tunable filter in the cavity. We used a CCD to capture the intensity distribution of the vortex beams emitted from the laser. Moreover, we additionally constructed a Michelson interferometer to detect the topological charge and to verify the helical wavefront of the generated vortex beam (Figure S6). Figure 3 illustrates the intensity distribution of the generated vortex beams and the interference patterns with Gaussian beam based on the four metasurfaces we fabricated. All the emitted vortex beams with $l = \pm 1$ have the doughnut-shaped intensity distribution with the same size, and the minimum intensity in the center forms a dark spot, which corresponds to the phase singularity. The right column of Figure 3 clearly shows the fork-shaped interference fringes. The number of fringes at the fork-shaped opening indicates that the absolute values of the topological charge of the vortex beams all satisfy $|l| = 1$, and the interference fringes with $l = 1$ and $l = -1$ have opposite opening directions, confirming successful design and manufacturing of the metasurfaces.

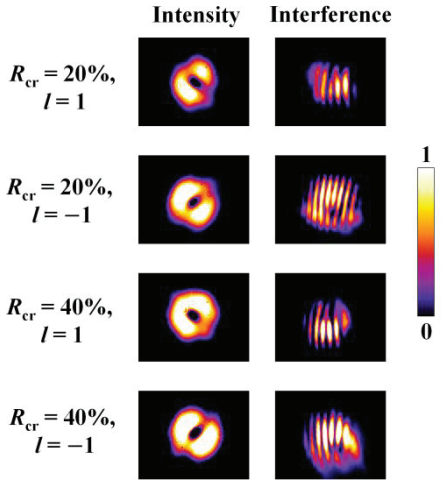

Figure 3. Measured intensity distribution and interference patterns of the output vortex beams generated in the laser with four fabricated metasurfaces inserted respectively.

We used an optical spectrum analyzer at the output port to monitor the spectrum of the vortex beam emitted from the laser. The lasing occurs at a central wavelength of about 1030 nm, predetermined by the gain spectrum of the Yb-PMF fiber. Figure 4 depicts the output power as

a function of the pump power of the vortex fiber laser based on the four metasurfaces. When the intracavity metasurfaces have the cross-polarized reflectivity of R_{cr} = 20%, the threshold pump power of the laser with l = 1 and –1 is 35 mW, and the slope efficiency of the corresponding output power relative to the pump power is 6.5% and 6.9%, respectively. In comparison, when the R_{cr} of the metasurfaces increases to 40%, the pump threshold of the laser with l = 1 and –1 increases to 41 mW and 40 mW, respectively, and the corresponding slope efficiencies increase as well, namely 14.8% and 14.4%. The phenomenon that larger pumping threshold and higher slope efficiency take place using metasurfaces with larger cross-polarization efficiency is very evident, and can be well understood by considering the relationship between gain and loss inside the cavity. Hence, one can design polarization conversion of the metasurfaces in real applications for vortex fiber lasers with lower lasing threshold, or larger output power, which are both important indicators for evaluating the performance of a laser.

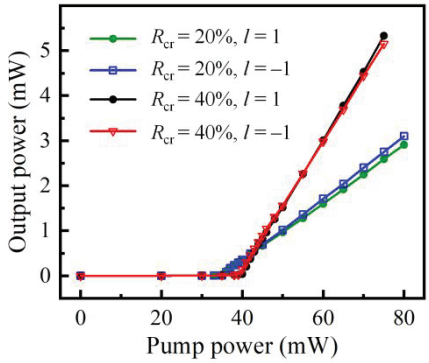

Figure 4. Evolution of the output power versus the pump power of the laser based on different metasurfaces.

In order to quantitatively characterize the OAM mode purity, we loaded helical phases of different topological charges on a spatial light modulator (SLM) to demodulate the OAM beams. The OAM beam emitted from the vortex laser was demodulated and reflected by the SLM, and finally projected onto the CCD camera (Figure S7). OAM mode purity is defined as the ratio of the relative central intensities of the beams after demodulation by helical phases with opposite topological charges.[60,61] The measured mode purities of the OAM beams with topological charges of $l = \pm 1$ output from the laser maintain around 90% (up to 93.8% for the best situation), all higher than the cases using metasurfaces outside the laser cavity (Table S2).

Wavelength Tunability of the Vortex Fiber Laser. The GSP metasurfaces can work at a relatively wide spectral range, as confirmed by Ref. 38, sufficient for a wavelength-tunable

vortex fiber laser, considering the finite gain bandwidth of the ytterbium-doped fiber. Firstly, taking the metasurfaces with R_{cr} = 40% as an example, we simulated the broadband characteristics of the designed GSP metasurface in the wavelength range from 1000 nm to 1100 nm. Figure 5a shows the evolution of the cross-polarized phase shift (φ_{cr}) of each metasurface unit with respect to the wavelength. With the increase of wavelength, the relative phase change of cross-polarization between adjacent metasurface units remains approximately constant ($\pi/4$), regardless of absolute variation. Therefore, a cross-polarized phase shift of 2π around a circumference can be obtained at each wavelength, which is a prerequisite for generating vortex beams with topological charge | l | = 1 in the broadband range. Besides, the cross-polarized reflectivity (R_{cr}) and the co-polarized reflectivity (R_{co}) of the eight units in this wavelength range were also calculated, as illustrated in Figure 5b,c. It is worth mentioning that each unit can still maintain R_{cr} of about 40% and relatively unchanged R_{co}, thereby enabling broadband control and generation of OAM beams in the laser.

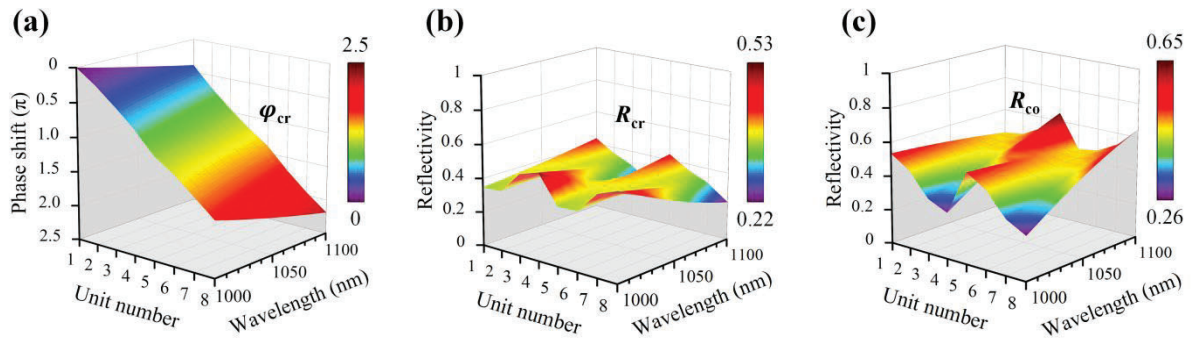

Figure 5. Simulated broadband characteristics of the metasurfaces with R_{cr} = 40% from 1000 nm to 1100 nm. (a) Cross-polarized phase shift (φ_{cr}) of eight units. (b) Cross-polarized reflectivity (R_{cr}) of eight units. (c) Co-polarized reflectivity (R_{co}) of eight units.

The tunable filter is then inserted into the metasurface-assisted vortex laser cavity. The wavelength of the emitted OAM beams from the fiber laser can be continuously adjusted by switching the center wavelength of the tunable filter. As shown in Figure 6, in the range from 1015 nm to 1075 nm, the laser could all emit well-defined vortex beams with | l | = 1. The intensity images and the interference fringes all confirm this. The pump threshold and the output power of the laser at different emission wavelengths are given in Figure 7a (taking the metasurface with R_{cr} = 40% for l = 1 as an example). At the pump power of 150 mW, we obtained the output power of the laser at different wavelengths. The fluctuations of the threshold pump power and output power reflect the differences of the losses in the laser cavity at different wavelengths. Furthermore, Figure 7b verifies that the variation of the operation wavelength

does not influence the OAM mode purity of the emitted beam. We should point out that the operation wavelength range of the fiber laser is narrower than the working bandwidth of the metasurfaces, which is mainly restricted by the limited spectral windows of other components in the cavity, in particular the operation bands of the collimator and the fiber mirror.

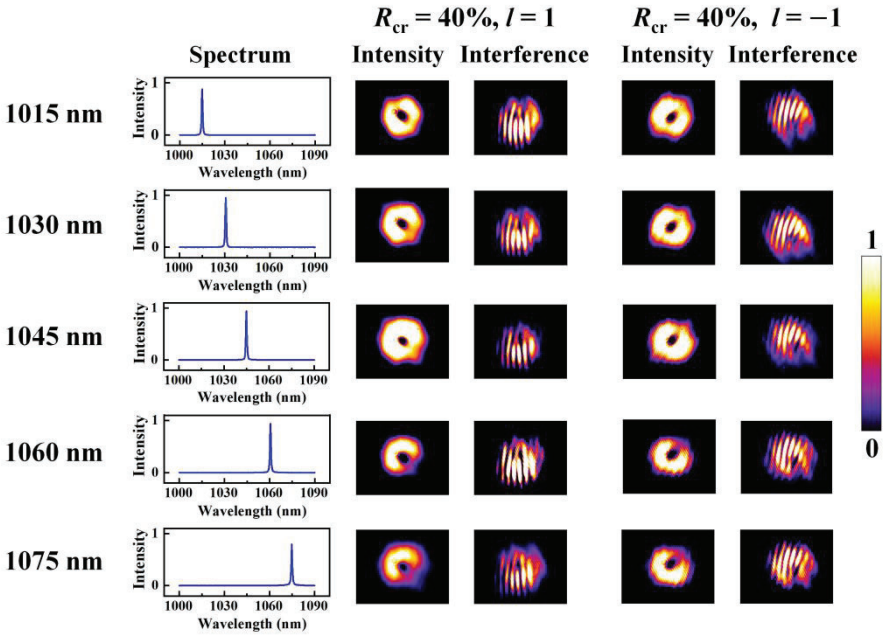

Figure 6. Experimental results of the broadband tunable characteristics of the vortex laser from 1015 nm to 1075 nm.

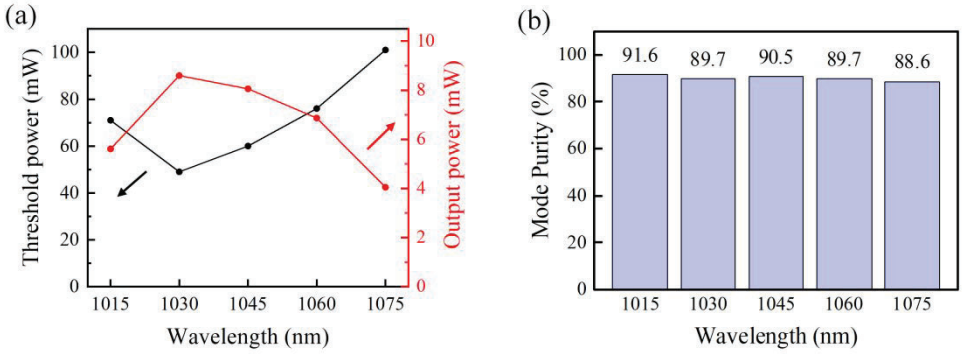

Figure 7. Pump threshold, output power, and mode purity of the vortex fiber laser as a function of emission wavelength. (a) Threshold pump power [black dots] and output power at the pump power of ~150 mW [red dots]. (b) OAM mode purity at different operation wavelengths. The metasurface with R_{cr} = 40% for l = 1 is employed.

Different from other reported vortex fiber lasers that employ mode-selective couplers, long-period fiber gratings, spatial light modulators, etc. for mode conversion, here we harness the

optical manipulation of metasurfaces. Thanks to the inherent flexibility and high efficiency of the GSP metasurfaces to shape light at will, one can tailor the nanostructures to exhibit broadband polarization conversion with controllable conversion ratio, particularly suitable for our vortex fiber laser design. In comparison to solid-state lasers, the single-mode fibers provide limited but really pure eigenmode, which enables very straightforward and effective control over mode numbers and mode purity. Combination of metasurfaces and fiber lasers could take the advantages of both, leading to flexible, simple, compact, and low-cost solutions. Due to the intrinsic high gain of fiber lasers, our laser cavity could endure large intracavity loss, basically extending the design space of the metasurfaces and versatility of output function. In addition, in our laser design, light passes the metasurfaces only once within a round-trip, avoiding the ambiguity of self-consistent propagation of laser modes, for example the case in Ref. 50, and allowing large insertion loss from the metasurfaces as well. The aforementioned aspects render our metasurface-based vortex fiber lasers close to practical applications for kinds of needs. In general, the design concept can be freely extended to generation of other structural beams. For instance, one can select proper unit cells to form new metasurfaces that help achieve higher-order OAM light, or other beams such as Airy beams. Furthermore, metasurfaces with different materials (metallic or dielectric metasurfaces) can also be engineered for generation of structured beams at various wavelengths (infrared, visible, etc), so as to enrich the performances and applications of metasurfaces-assisted vortex fiber lasers. Last but not least, one can also utilize active metasurfaces[62] to add reconfigurability and functionality of the structured-beam fiber laser sources.

CONCLUSION

In conclusion, we have proposed and demonstrated a compact wavelength-tunable vortex fiber laser by incorporating intracavity plasmon metasurfaces. Gained by the flexible and wideband optical manipulation of the metasurfaces, OAM beams of $l = \pm 1$ continuously tunable at the wavelength from 1015 nm to 1075 nm have been achieved in a low-cost and simple-configuration manner. The wavelength tunability is tens of nanometers broader than other vortex fiber lasers ever reported. Our implementation combines both advantages of fiber lasers and metasurfaces, broadening the strategy of OAM control directly at the sources, and can be extended to generate more complex structured beams. It could find potential applications including optical communications, quantum optics, super-resolution microscopy, and biophotonics.

METHODS

~~**Numerical Calculations.** The simulation of the metasurface units as shown in Figure 2(b) in this paper is based on the finite-element method (FEM). Floquet periodic boundary conditions (PBC) are applied to simulate an infinite array distribution. A linearly polarized beam is normally incident on the metasurface from a port defined by the air area (refractive index n = 1) above the metasurface. The top of the air layer above the metasurface is set as a perfectly matched layer (PML) that is no less than half wavelength ($\lambda/2$) to increase the absorption and avoid the influence of reflected light. The SiO_2 spacer layer of the metasurface is regarded as a lossless dielectric with refractive index n = 1.45. The permittivity of the Au nanorod and the Au thin film at the bottom is described by the Lorentz–Drude Model.[59]~~

■ ASSOCIATED CONTENT

Supporting Information

The Supporting Information is available free of charge via the Internet at http://pubs.acs.org.

Numerical calculations and optimization of nanorod dimensions for metasurfaces with different reflection efficiencies; the performances of the fabricated metasurfaces; SEM images and working efficiencies of the fabricated metasurfaces; the intensity of the co-polarized residual (CPR) beam; comparison of coupling efficiency between Gaussian beam and the co-polarized residual (CPR) beam; Detection of the topological charge of the OAM beams; and OAM mode purity characterization.

■ AUTHOR INFORMATION

Corresponding Authors

Lili Gui − State Key Laboratory of Information Photonics and Optical Communications, Beijing University of Posts and Telecommunications, Beijing 100876, China; orcid.org/0000-0002-3710-6330;

E-mail: liligui@bupt.edu.cn

Kun Xu − State Key Laboratory of Information Photonics and Optical Communications, Beijing University of Posts and Telecommunications, Beijing 100876, China;

E-mail: xukun@bupt.edu.cn

Authors

Chuanshuo Wang − State Key Laboratory of Information Photonics and Optical Communications, Beijing University of Posts and Telecommunications, Beijing 100876, China; Centre for Nano Optics, University of Southern Denmark, Campusvej 55, Odense M DK-5230, Denmark; orcid.org/0000-0003-0808-0431
Fei Ding − Centre for Nano Optics, University of Southern Denmark, Campusvej 55, Odense M DK-5230, Denmark; orcid.org/0000-0001-7362-519X
Hao Chen − State Key Laboratory of Information Photonics and Optical Communications, Beijing University of Posts and Telecommunications, Beijing 100876, China
Xiaosheng Xiao − State Key Laboratory of Information Photonics and Optical Communications, Beijing University of Posts and Telecommunications, Beijing 100876, China; orcid.org/0000-0002-9368-9956
Sergey I. Bozhevolnyi − Centre for Nano Optics, University of Southern Denmark, Campusvej 55, Odense M DK-5230, Denmark; orcid.org/0000-0002-0393-4859
Xiaoguang Zhang − State Key Laboratory of Information Photonics and Optical Communications, Beijing University of Posts and Telecommunications, Beijing 100876, China

Author Contributions

[†]L. Gui and C. Wang contributed equally to this work.

Funding

This work was funded by National Natural Science Foundation of China (61905018); Beijing Nova Program of Science and Technology (Z191100001119110); Fundamental Research Funds for the Central Universities (ZDYY202102-1); Fund of State Key Laboratory of Information Photonics and Optical Communications (Beijing University of Posts and Telecommunications) of China (IPOC2021ZR02 and IPOC2020ZT02); The Villum Kann Rasmussen Foundation (Award in Technical and Natural Sciences 2019); Villum Fonden (37372); Independent Research Fund Denmark (1134-00010B); The China Scholarship Council (No. 202206470038).

Notes

The authors declare no competing financial interest.

REFERENCES

(1) Allen, L.; Beijersbergen, M. W.; Spreeuw, R. J. C.; Woerdman, J. P. Orbital Angular Momentum of Light and the Transformation of Laguerre-Gaussian Laser Modes. *Phys. Rev. A* **1992**, *45*, 8185–8189.

(2) Shen, Y.; Wang, X.; Xie, Z.; Min, C.; Fu, X.; Liu, Q.; Gong, M.; Yuan, X. Optical Vortices 30 Years on: OAM Manipulation from Topological Charge to Multiple Singularities. *Light Sci. Appl.* **2019**, *8*, 90.

(3) Wang, J.; Yang, J.-Y.; Fazal, I. M.; Ahmed, N.; Yan, Y.; Huang, H.; Ren, Y.; Yue, Y.; Dolinar, S.; Tur, M.; Willner, A. E. Terabit Free-Space Data Transmission Employing Orbital Angular Momentum Multiplexing. *Nat. Photonics* **2012**, *6*, 488–496.

(4) Bozinovic, N.; Yue, Y.; Ren, Y.; Tur, M.; Kristensen, P.; Huang, H.; Willner, A. E.; Ramachandran, S. Terabit-Scale Orbital Angular Momentum Mode Division Multiplexing in Fibers. *Science* **2013**, *340*, 1545–1548.

(5) Lei, T.; Zhang, M.; Li, Y.; Jia, P.; Liu, G. N.; Xu, X.; Li, Z.; Min, C.; Lin, J.; Yu, C.; Niu, H.; Yuan, X. Massive Individual Orbital Angular Momentum Channels for Multiplexing Enabled by Dammann Gratings. *Light Sci. Appl.* **2015**, *4*, e257.

(6) Zhang, J.; Liu, J.; Shen, L.; Zhang, L.; Luo, J.; Liu, J.; Yu, S. Mode-Division Multiplexed Transmission of Wavelength-Division Multiplexing Signals over a 100-Km Single-Span Orbital Angular Momentum Fiber. *Photonics Res.* **2020**, *8*, 1236–1242.

(7) Willig, K. I.; Rizzoli, S. O.; Westphal, V.; Jahn, R.; Hell, S. W. STED Microscopy Reveals That Synaptotagmin Remains Clustered after Synaptic Vesicle Exocytosis. *Nature* **2006**, *440*, 935–939.

(8) Eggeling, C.; Ringemann, C.; Medda, R.; Schwarzmann, G.; Sandhoff, K.; Polyakova, S.; Belov, V. N.; Hein, B.; von Middendorff, C.; Schönle, A.; Hell, S. W. Direct Observation of the Nanoscale Dynamics of Membrane Lipids in a Living Cell. *Nature* **2009**, *457*, 1159–1162.

(9) Liang, L.; Feng, Z.; Zhang, Q.; Cong, T. D.; Wang, Y.; Qin, X.; Yi, Z.; Ang, M. J. Y.; Zhou, L.; Feng, H.; Xing, B.; Gu, M.; Li, X.; Liu, X. Continuous-Wave near-Infrared Stimulated-Emission Depletion Microscopy Using Downshifting Lanthanide Nanoparticles. *Nat. Nanotechnol.* **2021**, *16*, 975–980.

(10) Yu, W.; Ji, Z.; Dong, D.; Yang, X.; Xiao, Y.; Gong, Q.; Xi, P.; Shi, K. Super-Resolution Deep Imaging with Hollow Bessel Beam STED Microscopy. *Laser Photonics Rev.* **2016**, *10*, 147–152.

(11) Chapin, S. C.; Germain, V.; Dufresne, E. R. Automated Trapping, Assembly, and Sorting with Holographic Optical Tweezers. *Opt. Express* **2006**, *14*, 13095.

(12) Liu, C.; Guo, Z.; Li, Y.; Wang, X.; Qu, S. Manipulating Ellipsoidal Micro-Particles by Femtosecond Vortex Tweezers. *J. Opt.* **2015**, *17*, 035402.

(13) Zhang, Y.; Shi, W.; Shen, Z.; Man, Z.; Min, C.; Shen, J.; Zhu, S.; Urbach, H. P.; Yuan, X. A Plasmonic Spanner for Metal Particle Manipulation. *Sci. Rep.* **2015**, *5*, 15446.

(14) Liaw, J.-W.; Chien, C.-W.; Liu, K.-C.; Ku, Y.-C.; Kuo, M.-K. 3D Optical Vortex Trapping of Plasmonic Nanostructure. *Sci. Rep.* **2018**, *8*, 12673.

(15) Fickler, R.; Lapkiewicz, R.; Plick, W. N.; Krenn, M.; Schaeff, C.; Ramelow, S.; Zeilinger, A. Quantum Entanglement of High Angular Momenta. *Science* **2012**, *338*, 640–643.

(16) Fickler, R.; Campbell, G.; Buchler, B.; Lam, P. K.; Zeilinger, A. Quantum Entanglement of Angular Momentum States with Quantum Numbers up to 10,010. *Proc. Natl. Acad. Sci. U.S.A.* **2016**, *113*, 13642–13647.

(17) Ni, J.; Wang, C.; Zhang, C.; Hu, Y.; Yang, L.; Lao, Z.; Xu, B.; Li, J.; Wu, D.; Chu, J. Three-Dimensional Chiral Microstructures Fabricated by Structured Optical Vortices in Isotropic Material. *Light Sci. Appl.* **2017**, *6*, e17011.

(18) Harm, W.; Bernet, S.; Ritsch-Marte, M.; Harder, I.; Lindlein, N. Adjustable Diffractive Spiral Phase Plates. *Opt. Express* **2015**, *23*, 413.
(19) Sueda, K.; Miyaji, G.; Miyanaga, N.; Nakatsuka, M. Laguerre-Gaussian Beam Generated with a Multilevel Spiral Phase Plate for High Intensity Laser Pulses. *Opt. Express* **2004**, *12*, 3548–3553.
(20) Moreno, I.; Davis, J. A.; Pascoguin, B. M. L.; Mitry, M. J.; Cottrell, D. M. Vortex Sensing Diffraction Gratings. *Opt. Lett.* **2009**, *34*, 2927–2929.
(21) Stoyanov, L.; Topuzoski, S.; Stefanov, I.; Janicijevic, L.; Dreischuh, A. Far Field Diffraction of an Optical Vortex Beam by a Fork-Shaped Grating. *Opt. Commun.* **2015**, *350*, 301–308.
(22) Ostrovsky, A. S.; Rickenstorff-Parrao, C.; Arrizón, V. Generation of the "Perfect" Optical Vortex Using a Liquid-Crystal Spatial Light Modulator. *Opt. Lett.* **2013**, *38*, 534–536.
(23) Kumar, A.; Vaity, P.; Banerji, J.; Singh, R. P. Making an Optical Vortex and Its Copies Using a Single Spatial Light Modulator. *Phys. Lett. A* **2011**, *375*, 3634–3640.
(24) Marrucci, L.; Manzo, C.; Paparo, D. Optical Spin-to-Orbital Angular Momentum Conversion in Inhomogeneous Anisotropic Media. *Phys. Rev. Lett.* **2006**, *96*, 163905.
(25) JJ Nivas, J.; He, S.; Rubano, A.; Vecchione, A.; Paparo, D.; Marrucci, L.; Bruzzese, R.; Amoruso, S. Direct Femtosecond Laser Surface Structuring with Optical Vortex Beams Generated by a Q-Plate. *Sci. Rep.* **2015**, *5*, 17929.
(26) Yu, N.; Genevet, P.; Kats, M. A.; Aieta, F.; Tetienne, J.-P.; Capasso, F.; Gaburro, Z. Light Propagation with Phase Discontinuities: Generalized Laws of Reflection and Refraction. *Science* **2011**, *334*, 333–337.
(27) Sun, S.; He, Q.; Xiao, S.; Xu, Q.; Li, X.; Zhou, L. Gradient-Index Meta-Surfaces as a Bridge Linking Propagating Waves and Surface Waves. *Nat. Mater.* **2012**, *11*, 426–431.
(28) Kildishev, A. V.; Boltasseva, A.; Shalaev, V. M. Planar Photonics with Metasurfaces. *Science* **2013**, *339*, 1232009.
(29) Zheng, G.; Mühlenbernd, H.; Kenney, M.; Li, G.; Zentgraf, T.; Zhang, S. Metasurface Holograms Reaching 80% Efficiency. *Nat. Nanotechnol.* **2015**, *10*, 308–312.
(30) Wang, S.; Wu, P. C.; Su, V.-C.; Lai, Y.-C.; Hung Chu, C.; Chen, J.-W.; Lu, S.-H.; Chen, J.; Xu, B.; Kuan, C.-H.; Li, T.; Zhu, S.; Tsai, D. P. Broadband Achromatic Optical Metasurface Devices. *Nat. Commun.* **2017**, *8*, 187.
(31) Ren, H.; Briere, G.; Fang, X.; Ni, P.; Sawant, R.; Héron, S.; Chenot, S.; Vézian, S.; Damilano, B.; Brändli, V.; Maier, S. A.; Genevet, P. Metasurface Orbital Angular Momentum Holography. *Nat. Commun.* **2019**, *10*, 2986.
(32) Huang, L.; Chen, X.; Mühlenbernd, H.; Li, G.; Bai, B.; Tan, Q.; Jin, G.; Zentgraf, T.; Zhang, S. Dispersionless Phase Discontinuities for Controlling Light Propagation. *Nano Lett.* **2012**, *12*, 5750–5755.
(33) Karimi, E.; Schulz, S. A.; De Leon, I.; Qassim, H.; Upham, J.; Boyd, R. W. Generating Optical Orbital Angular Momentum at Visible Wavelengths Using a Plasmonic Metasurface. *Light Sci. Appl.* **2014**, *3*, e167.
(34) Arbabi, A.; Horie, Y.; Bagheri, M.; Faraon, A. Dielectric Metasurfaces for Complete Control of Phase and Polarization with Subwavelength Spatial Resolution and High Transmission. *Nat. Nanotechnol.* **2015**, *10*, 937–943.
(35) Devlin, R. C.; Ambrosio, A.; Wintz, D.; Oscurato, S. L.; Zhu, A. Y.; Khorasaninejad, M.; Oh, J.; Maddalena, P.; Capasso, F. Spin-to-Orbital Angular Momentum Conversion in Dielectric Metasurfaces. *Opt. Express* **2017**, *25*, 377–393.
(36) Hu, Y.; Liu, X.; Jin, M.; Tang, Y.; Zhang, X.; Li, K. F.; Zhao, Y.; Li, G.; Zhou, J. Dielectric Metasurface Zone Plate for the Generation of Focusing Vortex Beams. *PhotoniX* **2021**, *2*, 10.

(37) Yue, F.; Wen, D.; Xin, J.; Gerardot, B. D.; Li, J.; Chen, X. Vector Vortex Beam Generation with a Single Plasmonic Metasurface. *ACS Photonics* **2016**, *3*, 1558–1563.
(38) Ding, F.; Chen, Y.; Bozhevolnyi, S. I. Focused Vortex-Beam Generation Using Gap-Surface Plasmon Metasurfaces. *Nanophotonics* **2020**, *9*, 371–378.
(39) Heiden, J. T.; Ding, F.; Linnet, J.; Yang, Y.; Beermann, J.; Bozhevolnyi, S. I. Gap-Surface Plasmon Metasurfaces for Broadband Circular-to-Linear Polarization Conversion and Vector Vortex Beam Generation. *Adv. Opt. Mater.* **2019**, *7*, 1801414.
(40) Wang, J. Metasurfaces Enabling Structured Light Manipulation: Advances and Perspectives. *Chin. Opt. Lett.* **2018**, *16*, 050006.
(41) Forbes, A. Structured Light from Lasers. *Laser Photonics Rev.* **2019**, *13*, 1900140.
(42) Zhang, Z.; Qiao, X.; Midya, B.; Liu, K.; Sun, J.; Wu, T.; Liu, W.; Agarwal, R.; Jornet, J. M.; Longhi, S.; Litchinitser, N. M.; Feng, L. Tunable Topological Charge Vortex Microlaser. *Science* **2020**, *368*, 760–763.
(43) Ngcobo, S.; Litvin, I.; Burger, L.; Forbes, A. A Digital Laser for On-Demand Laser Modes. *Nat. Commun.* **2013**, *4*, 2289.
(44) Naidoo, D.; Roux, F. S.; Dudley, A.; Litvin, I.; Piccirillo, B.; Marrucci, L.; Forbes, A. Controlled Generation of Higher-Order Poincaré Sphere Beams from a Laser. *Nat. Photonics* **2016**, *10*, 327–332.
(45) Wei, D.; Cheng, Y.; Ni, R.; Zhang, Y.; Hu, X.; Zhu, S.; Xiao, M. Generating Controllable Laguerre-Gaussian Laser Modes through Intracavity Spin-Orbital Angular Momentum Conversion of Light. *Phys. Rev. Appl.* **2019**, *11*, 014038.
(46) Wang, T.; Wang, F.; Shi, F.; Pang, F.; Huang, S.; Wang, T.; Zeng, X. Generation of Femtosecond Optical Vortex Beams in All-Fiber Mode-Locked Fiber Laser Using Mode Selective Coupler. *J. Light. Technol.* **2017**, *35*, 2161–2166.
(47) Zhou, N.; Liu, J.; Wang, J. Reconfigurable and Tunable Twisted Light Laser. *Sci. Rep.* **2018**, *8*, 11394.
(48) Zhou, N.; Wang, J. Metasurface-Assisted Orbital Angular Momentum Carrying Bessel-Gaussian Laser: Proposal and Simulation. *Sci. Rep.* **2018**, *8*, 8038.
(49) Chriki, R.; Maguid, E.; Tradonsky, C.; Kleiner, V.; Friesem, A. A.; Davidson, N.; Hasman, E. Spin-Controlled Twisted Laser Beams: Intra-Cavity Multi-Tasking Geometric Phase Metasurfaces. *Opt. Express* **2018**, *26*, 905.
(50) Sroor, H.; Huang, Y.-W.; Sephton, B.; Naidoo, D.; Vallés, A.; Ginis, V.; Qiu, C.-W.; Ambrosio, A.; Capasso, F.; Forbes, A. High-Purity Orbital Angular Momentum States from a Visible Metasurface Laser. *Nat. Photonics* **2020**, *14*, 498–503.
(51) Mao, D.; Zheng, Y.; Zeng, C.; Lu, H.; Wang, C.; Zhang, H.; Zhang, W.; Mei, T.; Zhao, J. Generation of Polarization and Phase Singular Beams in Fibers and Fiber Lasers. *Adv. Photonics* **2021**, *3*, 014002.
(52) Wang, T.; Wu, J.; Wu, H.; Wang, J.; Huang, L.; Zhou, P. Wavelength-Tunable LP11 Mode Pulse Fiber Laser Based on Black Phosphorus. *Opt. Laser Technol.* **2019**, *119*, 105618.
(53) Wan, H.; Wang, J.; Zhang, Z.; Cai, Y.; Sun, B.; Zhang, L. High Efficiency Mode-Locked, Cylindrical Vector Beam Fiber Laser Based on a Mode Selective Coupler. *Opt. Express* **2017**, *25*, 11444–11451.
(54) Dong, Z.; Sun, H.; Zhang, Y.; Zou, J.; Xu, L.; Luo, Z. Visible-Wavelength-Tunable, Vortex-Beam Fiber Laser Based on a Long-Period Fiber Grating. *IEEE Photonics Technol. Lett.* **2021**, *33*, 1173–1176.
(55) Zhang, T.; Hu, H.; Chen, J.; Zhan, Q. Tunable Mode-Locked Fiber Laser to Generate Ultrashort Cylindrical Vector Beams. *Laser Phys. Lett.* **2021**, *18*, 035102.
(56) Lin, J.; Yan, K.; Zhou, Y.; Xu, L. X.; Gu, C.; Zhan, Q. W. Tungsten Disulphide Based All Fiber Q-Switching Cylindrical-Vector Beam Generation. *Appl. Phys. Lett.* **2015**, *107*, 191108.

(57) Wang, J.; Zhang, J.; Wang, A.; Jiang, X.; Yao, J.; Zhan, Q. Cascaded Stimulated Brillouin Scattering Erbium-Doped Fiber Laser Generating Orbital Angular Momentum Beams at Tunable Wavelengths. *Opt. Express* **2021**, *29*, 18408–18419.
(58) Grady, N. K.; Heyes, J. E.; Chowdhury, D. R.; Zeng, Y.; Reiten, M. T.; Azad, A. K.; Taylor, A. J.; Dalvit, D. A. R.; Chen, H.-T. Terahertz Metamaterials for Linear Polarization Conversion and Anomalous Refraction. *Science* **2013**, *340*, 1304–1307.
(59) Rakić, A. D.; Djurišić, A. B.; Elazar, J. M.; Majewski, M. L. Optical Properties of Metallic Films for Vertical-Cavity Optoelectronic Devices. *Appl. Opt.* **1998**, *37*, 5271–5283.
(60) Zhang, J.; Sun, C.; Xiong, B.; Wang, J.; Hao, Z.; Wang, L.; Han, Y.; Li, H.; Luo, Y.; Xiao, Y.; Yu, C.; Tanemura, T.; Nakano, Y.; Li, S.; Cai, X.; Yu, S. An InP-Based Vortex Beam Emitter with Monolithically Integrated Laser. *Nat. Commun.* **2018**, *9*, 2652.
(61) Wu, C.; Kumar, S.; Kan, Y.; Komisar, D.; Wang, Z.; Bozhevolnyi, S. I.; Ding, F. Room-Temperature on-Chip Orbital Angular Momentum Single-Photon Sources. *Sci. Adv.* **2022**, *8*, eabk3075.
(62) Meng, C.; Thrane, P. C. V.; Ding, F.; Gjessing, J.; Thomaschewski, M.; Wu, C.; Dirdal, C.; Bozhevolnyi, S. I. Dynamic Piezoelectric MEMS-Based Optical Metasurfaces. *Sci. Adv.* **2021**, *7*, eabg5639.